J. Phys. Chem. A **2003,** *107,* 8239−8250

Analysis of Hydrogen Atom Transfer in Photoexcited Indole$(NH_3)_n$ Clusters by Femtosecond Time-Resolved Photoelectron Spectroscopy[†]

H. Lippert, V. Stert, L. Hesse, C. P. Schulz, I. V. Hertel,[‡] and W. Radloff*

Max Born Institute, Max-Born-Strasse 2A, D-12489 Berlin-Adlershof, Germany

Received: December 13, 2002; In Final Form: April 8, 2003

The photoinduced H-atom-transfer reaction in indole$(NH_3)_n$ clusters has been analyzed by femtosecond time-resolved photoelectron−photoion coincidence spectroscopy. The different contributions to the measured time-dependent ion and electron signals resulting from ionization by one and two probe photons can be discriminated and analyzed separately. In particular, the distinctively different dynamical behavior observed for clusters with small ($n = 1-3$) and larger ($n \geq 4$) numbers of ammonia molecules is elucidated. For the small clusters an ultrafast process with a time constant of about 150 fs is identified and attributed to internal conversion from the initially excited $\pi\pi^*$ state to the $\pi\sigma^*$ state. In contrast, for the larger clusters ($n \geq 4$) such an initial ultrafast process is not observable probably for Franck−Condon reasons, while a structural rearrangement mechanism after the H transfer on a time scale of 10 ps is clearly recognized.

I. Introduction

With femtosecond spectroscopy and the methods of cluster science it is possible to approach a detailed understanding of the photochemistry of amino acids embedded in a well-defined number of polar molecules such as water or ammonia, i.e., as a function of the microenvironment. As a starting point toward such a systematic study of size-selective and site-specific dynamics and energetics of the building blocks of life, we report here the first time-resolved photoelectron spectra of indole, the chromophore of tryptophan, in an environment of a few ammonia molecules prepared in a molecular beam experiment. Photoexcitation of indole in aqueous solution leads to charge separation and the formation of a solvated electron, processes typical in this type of system (see, e.g., refs 1 and 2). Molecular beam experiments with clusters allow one to trace the evolution of these characteristic processes with the size of the solvation shell.

Recent ab initio calculations of the potential energy surfaces of the free indole molecule[3] and indole−water clusters[4] have shown that a low-lying $\pi\sigma^*$ Rydberg-type state of the indole molecule plays the crucial role in the photophysics, because in this state a large amount of the electronic charge is displaced along the N−H coordinate toward the H atom. In indole−water clusters the electron charge is completely separated from the indole molecule and solvated by the water molecules. The $\pi\sigma^*$ state of indole is a dark state but can be populated by nonadiabatic coupling to the optically accessible $\pi\pi^*$ states of the molecule. Direct experimental evidence for the $\pi\sigma^*$ state has been given very recently.[5]

As analogous theoretical studies of the similar systems of phenol−water and phenol−ammonia clusters have shown,[6] the photoinitiated internal conversion leads to a fast hydrogen atom transfer. For phenol−ammonia clusters this has been confirmed experimentally in the groups of Jouvet[7] and Fujii.[8] It is suggested that such a H-transfer reaction also characterizes the photochemistry in indole−water and indole−ammonia clusters.[9] Indeed, the first pump−probe experiments with indole−ammonia clusters have confirmed this expectation. By applying nanosecond laser pulses at 272 nm (pump pulse) and at 355 nm (probe pulse), $(NH_3)_{n-1}NH_4^+$ ions have been observed for pump−probe delay times up to 800 ns, indicating the formation of the long-living neutral species by a dissociative H-transfer reaction[10] of the indole−ammonia clusters (in the following denoted by $IndNH(NH_3)_n$) which—very schematically—may be characterized as

$$\xrightarrow{272\ \text{nm}} \mathrm{IndNH(NH_3)_n}^* \rightarrow \mathrm{IndN(NH_3)_{n-1}NH_4} \rightarrow \mathrm{IndN} + \mathrm{(NH_3)_{n-1}NH_4} \quad (1)$$

During the past few years a wealth of spectroscopic data for indole in clusters of polar molecules have been reported (see, e.g., ref 11 and references therein). But only very recently the first time-resolved investigations were reported. In a pump−probe experiment with femtosecond laser pulses we have studied the dynamics in excited indole−ammonia clusters by analyzing the time-dependent ion signals of the parent clusters[12] and the ammonium product radicals.[13] The clusters were excited to the $S_1(\pi\pi^*)$ state by pump pulses at a wavelength of 263 nm (4.71 eV). The dynamics was probed by photoionization of the excited parent clusters as well as the product clusters with probe photons at 395 nm (3.14 eV). An ultrafast process on the time scale of a few hundred femtoseconds and a slow decay process with time constants of several tens of picoseconds were observed for small $IndNH(NH_3)_n$ clusters ($n = 1-3$), while the situation changed dramatically for $n \geq 4$. Tentatively, the ultrafast decay was interpreted as being due to internal conversion from the $\pi\pi^*$ state to the $\pi\sigma^*$ state, while the decay on the picosecond time scale was attributed to a substantial internal rearrangement of the cluster structure after the H transfer.[12] On a still longer time scale (75−200 ps) the formation of fragment radicals was observed.[13]

[†] Part of the special issue "A. C. Albrecht Memorial Issue".

[*] To whom correspondence should be addressed. E-mail: radloff@mbi-berlin.de.

[‡] Also at Fachbereich Physik, Freie Universität Berlin. URL: http://staff.mbi-berlin.de/hertel.

10.1021/jp0277098 CCC: $25.00

Obviously, to understand the photoinduced processes in their full complexity, we need additional information. In the present work we resort to photoelectron spectroscopy. We have applied the femtosecond time-resolved electron−ion coincidence (FEICO) detection method[14] to study the dynamics in excited indole−ammonia clusters, correlating the energy of a detected photoelectron unambiguously to a cluster ion of specific size n from which it was ejected—parent ion $IndNH(NH_3)_n^+$ as well as radical product ion $(NH_3)_{n-1}NH_4^+$. Photoelectron spectra add one further dimension of information to probing the time evolution of a photoexcited system and will allow us to some extent to map out the reaction path—or more precisely the change in Franck−Condon overlap regions between the excited neutral and the ionic states as the system undergoes nonadiabatic transitions and internal rearrangement of its constituents. Of particular and general interest is proton or hydrogen transfer within the system and the pathways to the formation of the reaction products as indicated by eq 1. We find characteristic changes in the photoelectron spectra on the femto- and picosecond time scales and discuss these in terms of different types of processes involved.

II. Experimental Setup

The experimental setup is similar to that used in previous experiments (see, e.g., ref 14). The indole−ammonia clusters are formed by a free adiabatic expansion of a gas mixture through a pulsed nozzle. The gas mixture (backing pressure 1 bar) contains indole vapor (vapor pressure at about 30 °C) and ammonia (0.4−3%) in He or Ar seed gas. Due to the low indole concentration no indole clusters are obtained in the molecular beam. The molecular beam is crossed by two weakly focused copropagating laser beams in the extraction region of a combined ion mass and electron time-of-flight (TOF) spectrometer. The $IndNH(NH_3)_n$ cluster size distribution in the interaction zone can be controlled by the ammonia concentration in the gas mixture as well as by irradiating the molecular beam pulse in its front region where the cluster formation is just starting. Typically, two different adjustments were used, leading to a “broad” cluster distribution with $n \leq 6$ (ammonia concentration 3%) and a “narrow” one with $n \leq 2$ (ammonia concentration 0.4%). The respective typical mass spectra are shown in Figure 1.

The laser system used is a commercial Ti:sapphire laser and amplifier system (Clark MXR) tuned to 790 nm. The third harmonics of the fundamental wave at $\lambda_1 = 263$ nm (4.71 eV) is used to pump the clusters, whereas the second harmonics at $\lambda_2 = 395$ nm (3.14 eV) is applied to probe the excited clusters as well as the reaction products by ionization. The width of the laser pulses is about 140 fs. When only ion signals as a function of the pump−probe time delay are recorded, we typically use laser fluences of 0.5 and 5 mJ/cm^2 for the pump and probe pulses, respectively.

To record mass-specific photoelectron spectra of the indole−ammonia clusters, we have to apply the FEICO technique,[14] a method which has by now proven very useful for studying ultrafast dynamics in a variety of molecular and cluster systems. Briefly, the ions are detected by a Wiley−McLaren-type TOF mass spectrometer, while the corresponding photoelectrons are analyzed by a “magnetic bottle” TOF electron spectrometer. The energy resolution of the electron spectrometer for the low-energy electrons detected here is about 30 meV. The ion and electron signals are registered in a multihit time-to-digital converter (Le Croy 4208) which is started by the laser pulses. The FEICO signals are stored and analyzed by a PC. To keep the contribution of uncorrelated coincidences sufficiently low, we have strongly reduced the laser fluences, with total ionization rates of only 0.05−0.10 per laser pulse.[14]

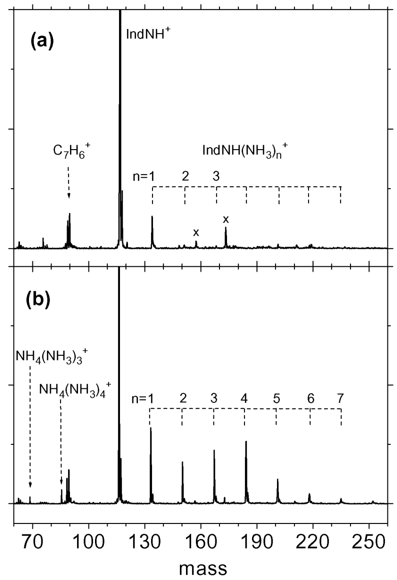

Figure 1. Mass spectra observed at the delay time $\tau = 300$ ps for (a) narrow ($n \leq 2$) and (b) broad ($n \leq 6$) cluster distributions. The mass peak of $C_7H_6^+$ represents an indole fragment. The additional peaks (×) in (a) are due to one Ar atom bound to indole and indole(NH_3).

A standard delay line is used to scan the delay time between the pump and the probe pulses. At a repetition frequency of 1 kHz the electron spectra are accumulated typically for 3×10^4 laser pulses at each delay time τ and averaged over about 70 up- and down-scans of the delay line.

III. Experimental Results and Discussion

We have recorded both the ion-signal delay time scans and the FEICO electron spectra with the narrow and the broad cluster distributions. While for the data recorded with the narrow distribution congestions of the signals due to ionic fragments from larger clusters are minimized, the broad cluster distribution allows us to study the dynamics as a function of cluster size and at the same time to glean information on these ionic fragmentation channels in a controlled manner. In Figure 1 typical mass spectra of $IndNH(NH_3)_n$ are shown as obtained for the narrow (Figure 1a) and the broad (Figure 1b) cluster distributions at a delay time of $\tau = 300$ ps between the pump pulse at 263 nm and the probe pulse at 395 nm. For the narrow distribution clusters up to $n \leq 2$ can be recognized, whereas the broad distribution allows the investigation of clusters up to $n = 6$. For the narrow distribution, the total rate of photoion−photoelectron coincidences is maintained at about 0.05 per pulse so that false coincidences at $\tau = 0$ due to the very strong electron signal of NH_3^+ are completely avoided and no correction is necessary. A small contribution of false coincidences to the spectra for the broad distribution—showing up in particular at $\tau = 0$ due to the strong ammonia monomer signal—has been corrected for (see ref 14). In the mass spectrum of the broad distribution (Figure 1b) we also see several product radical ions $(NH_3)_{n-1}NH_4^+$ for $n \geq 4$. The probe pulse energy at a wavelength of 395 nm (3.14 eV) is not sufficient to ionize smaller ammonium radicals; their formation has, however, been firmly established by three-photon ionization using high probe beam intensities at a probe wavelength of 790 nm (1.57 eV).[13]

A. Ion Signals. For a concise discussion we briefly recall some of the previous results. Time-dependent $IndNH(NH_3)_n^+$

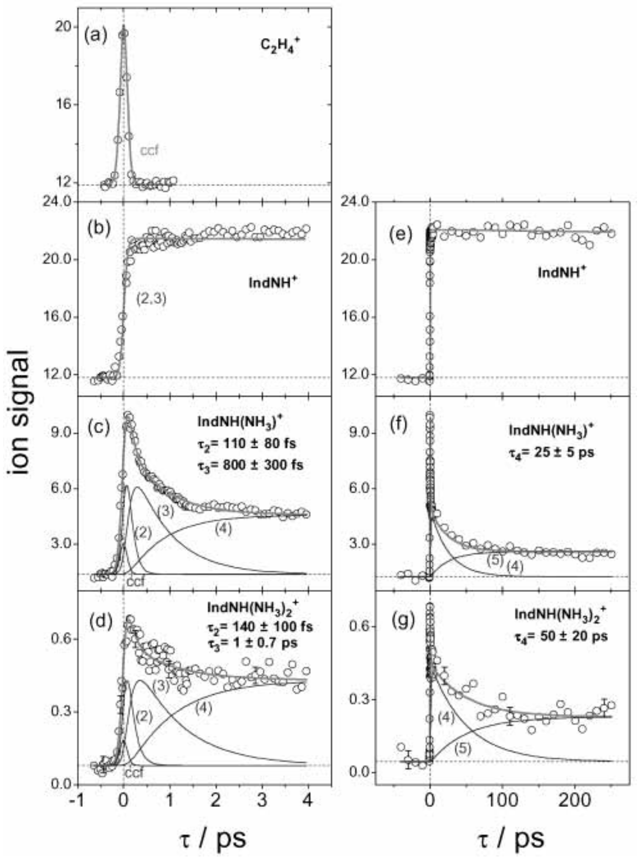

Figure 2. Indole(NH_3)$_n^+$, $n = 0-2$, ion signals from the narrow distribution at short (b−d) and long (e−g) delay times τ between pump (263 nm) and probe (395 nm) pulses. Zero time delay and the width of the cross correlation function have been derived from comparison with nonresonantly ionized C_2H_4 molecules as shown in panel a. The experimental curves are fitted according to the Bloch and kinetic models described in section III.B. The different contributions (numbers in parentheses) correspond to the configurations indicated in Figure 6. A nonresonant contribution (ccf) has to be added to obtain satisfactory agreement with the data at time delay zero. The ion signals are given in arbitrary units, with short (left panels) and longer (right panels) delay times being normalized to each other.

ion signals after excitation of the $\pi\pi^*$ state with $h\nu_{pu}$ and ionization by one probe photon $h\nu_{pr}$ (and also by $2h\nu_{pr}$ as we shall see in section III.C) are shown in Figure 2 for parent ion signals up to $n = 2$ obtained from the narrow cluster distribution. Figure 3 shows the corresponding data from a broad cluster distribution. The previously reported set of data[12] has been extended for clusters up to $n = 6$, and in addition to the time evolution on a longer time scale ($\tau < 250$ ps), we report now for all cluster sizes also delay scans on a short time scale ($\tau < 2.5$ ps). All data are fitted with a consistent kinetic model described in section III.B. For the ultrafast dynamics (left panels in Figures 2 and 3) we have used optical Bloch equations combined with rate equations.[15] As indicated by the components of the fit curves shown in Figure 2 our data forced us to assume two kinetic steps following the initial excitation of the $\pi\pi^*$ state (2)—labeled 3 and 4—to fit the data sufficiently well. This will be rationalized in section III.B. The ion signals at longer delay times (right panels) were fitted by a single-exponential decay (rise) function of the type

$$I(\tau) = a\exp(-\tau/\tau_4) + b[1 - \exp(-\tau/\tau_4)] \qquad (2)$$

reflecting the decay of configuration 4 and the rise of a further configuration (5). The fits for short delay times and long delay times are normalized to each other.

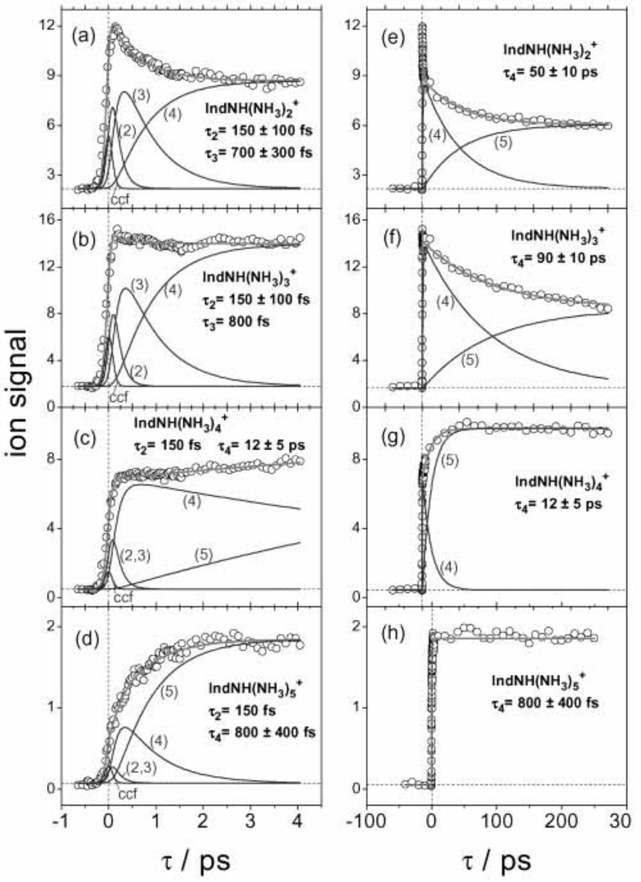

Figure 3. Indole(NH_3)$_n^+$, $n = 2-5$, ion signals obtained from a broad cluster distribution ($n \leq 6$) vs delay time τ with fits to the kinetic model. Otherwise as Figure 2.

The experimental determination of zero delay time was done using the $C_2H_4^+$ ion signal, which is obtained from a nonresonant multiphoton ionization process. As illustrated in Figure 2a this signal also allows us to monitor the effective cross correlation function (ccf) of our pump−probe laser pulse setup. The Bloch equation fit predicts for a purely resonant excitation of the $\pi\pi^*$ state (without dephasing) a rise time which is somewhat shifted toward positive delay times with respect to the cross correlation function (for details see ref 15). In contrast, all our experimental data in the present case show that the ion signal rises nearly as fast as the ccf signal (Figure 2a). Such behavior may be caused either by an incoherent contribution to the ion signal or by nonresonant multiphoton ionization at $\tau = 0$ (possibly by one probe photon and one pump photon). We find that taking only the ccf contribution into account leads to satisfactory fits; i.e., this rapid rise of the ion signal does not necessarily reflect any dynamics of the excited state. However, the excited-state dynamics is clearly reflected in the ion signal at $\tau > 100$ fs after this initial very fast rise: we observe for $n = 1$ and 2 (Figure 2) an ultrafast decay with τ_2 slightly above 100 fs, followed by a slower decay with time constant $\tau_3 \approx 800$ fs. The subsequent much slower decay occurs on a time scale of 25−300 ps, with time constant τ_4 slightly increasing with larger cluster size. This indicates $a > b$ in eq 2. It is important to note at this point that the coefficients a and b reflect a convolution of the excited-state population probability in a particular configuration (4 and 5, respectively) with the probability to ionize it. Both quantities may change with time, which makes the interpretation of the experimental data even more complex. A similar argument holds for the population, depopulation, and detection of the excited system on the ultrafast time scale.

As seen, the ion signal for $n = 2$ is rather weak for the narrow cluster distribution, which was chosen to minimize fragmentation. To study larger clusters, we must recur to the broad cluster distribution (Figure 3). The resulting fragmentation is reflected in an apparent increase of the ratio b/a (eq 2). For $n = 1$ it changes from 0.35 to 0.6 (not shown here) and for $n = 2$ from 0.4 to 0.6 (cf. parts g and e of Figure 2).

The fact that the change between narrow and broad cluster distributions for $n = 2$ is only about 50% and apparently decreases with cluster size gives us some confidence in assuming that fragmentation does not obscure the main features for the dynamics on the exited state to be discussed below. Clearly, the trend for the dynamics observed at $n = 1$ and 2 in Figure 2 is seen to continue for $n = 2$ and 3 in Figure 3. In contrast, for the larger clusters the ion signals do not decay—neither on the femtosecond nor on the picosecond time scale. Instead, the signals rise with time constant $\tau_4 \approx 12$ ps for $n = 4$ (Figure 3c,g) and even faster for $n = 5$ (Figure 3d,h) and 6 (not shown here); with reference to eq 2 this implies $a \lesssim b$, which we have to interpret as an increase of the detection probabilities as the dynamics evolves on the excited state of the clusters with $n \geq 4$. A word of caution about the determination of τ_2 and τ_3 is appropriate: the values given in Figure 3b–d are somewhat arbitrary for $n > 2$ as indicated by the fitting contributions shown. When $a \lesssim b$, i.e., for the larger clusters, $n \geq 4$, it cannot be determined at all: although there may be significant dynamics on the short time scale, it cannot be measured by the present method.

Table 1 summarizes the time constants as derived from the ion signals. They are consistent with the dynamics seen in the FEICO spectra as discussed in section III.C.

In addition, the formation times for the product radicals are also reported in Table 1. Two examples of the respective ion scans are shown in Figure 4 as obtained for long delay times from the broad cluster distribution (cf. Figure 1b). These signals also rise from zero but with a much longer time constant than the respective cluster ions. The solid lines are again single-exponential fits to the measured data points, in this case with $a = 0$ and τ_4 replaced by τ_f in eq 2. Note that the ions detected on the product mass arise from ionization of neutral radicals $(NH_3)_{n-1}NH_4$ formed by dissociation of $IndNH(NH_3)_n$ in the excited state as indicated by eq 1—and not from fragmentation in the ionic state.[13]

For several reasons the time constants given in Table 1, in particular τ_2 and τ_3, are subject to relatively large statistical and systematic errors. They are estimates derived from several data sets with varying input and detection parameters.

(i) We must be aware that all ion signals shown in Figures 2 and 3 may to some extent be obscured by a certain amount of fragmentation in the ionic system, i.e., by reactions of the type

$$\mathrm{IndNH(NH_3)}_n^+ \rightarrow \mathrm{IndNH(NH_3)}_{n-x}^+ + x(\mathrm{NH_3}) \tag{3}$$

which can occur a long time (several nanoseconds to many microseconds) after ionization and are unrelated to the rearrangement and dissociation processes in the excited states, which are our primary concern. Evidence for this has been discussed above. Even though with the narrow cluster distribution we try to minimize these contributions from ion fragmentation, we cannot completely rule out any influence of it on the ion and electron signals.

TABLE 1: Experimentally Determined Time Scales for $IndNH(NH_3)_n$ Excited-State Reactions[a]

n	τ_2/fs	τ_3/ps	τ_4/ps	product	τ_f/ps
0	nd[b]				
1	150 ± 100	0.7 ± 0.3	35 ± 15	NH_4 (weak)	
2	150 ± 100	0.7 ± 0.3	55 ± 15	NH_3NH_4	160 ± 40
3	150 ± 100	~0.8	90 ± 10	$(NH_3)_2NH_4$	125 ± 20
4	~150	nd[b]	12 ± 5	$(NH_3)_3NH_4$	130 ± 20
5	~150	nd[b]	0.8 ± 0.4	$(NH_3)_4NH_4$	80 ± 20
6	~150	nd[b]	0.6 ± 0.3	$(NH_3)_5NH_4$	75 ± 10

[a] τ_2 = time constant for internal conversion $\pi\pi^* \rightarrow \pi\sigma^*$, τ_3 = time constant for initial rearrangement in $\pi\sigma^*$, τ_4 = H relaxation time to equilibrium state $IndN(NH_3)_{n-1}NH_4$, and τ_f = product formation time. [b] nd = cannot be determined from experiment.

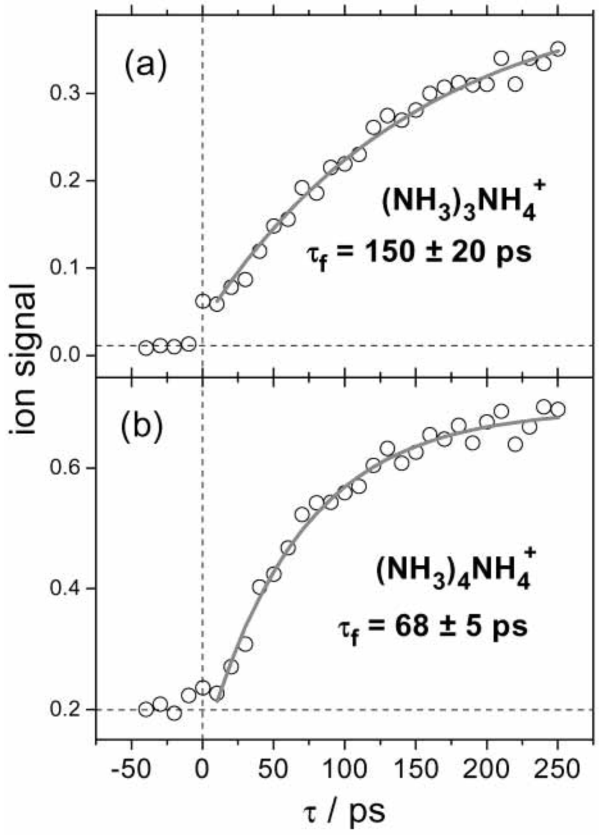

Figure 4. Ion signals $(NH_3)_{n-1}NH_4^+$, $n = 4$ and 5, from the excited-state reaction products obtained from a broad indole$(NH_3)_n$ cluster distribution ($n \leq 6$) vs delay time τ and fit to a single-exponential growth function ($a = 0$ in eq 2). Otherwise as Figure 2.

(ii) As we shall see, one-photon ionization and ionization by two probe photons contribute to the ion signals detected. Since the relative fraction of the two signals depends strongly on the absolute intensity of the probe laser pulse, we have to carefully analyze the data to disentangle these contributions, as discussed in section III.C.

(iii) The time evolution of the ion signal reflects the probability to find the clusters at a specific place on the excited-state potential energy surface(s), the density of states in the excited and ionic states, and the Franck–Condon factor for the overlap between excited states and ionic states. In other words, the factors a and b in eq 2 are a complex convolution of the excited-state population and their detection efficiency at a given laser intensity. If, e.g., the detection probabilities for an initial state and a final state are identical, a transition between these states cannot be detected in our ion signals.

We have repeated the present experiments with a number of initial conditions and laser intensities. The range of time constants given in Table 1 gives the systematic errors thus estimated. The numbers obtained can be interpreted in terms of the kinetic model described in section III.B. The FEICO

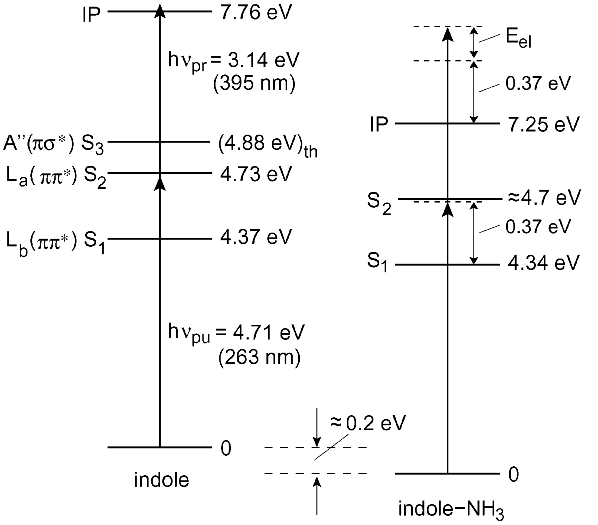

Figure 5. Energy scheme of indole and indole(NH_3) for vertical transitions from the equilibrium ground state. Also shown are the energies of the pump ($h\nu_{pu}$) and probe ($h\nu_{pr}$) photons and the expected electron energies.

electron spectra discussed in section III.C will finally allow us to understand the underlying dynamics much better and corroborate the interpretation used to fit the ion signals obtained from the pump−probe delay scans.

B. Kinetic Model. The interpretation of the electron spectra will be based on the experimental and theoretical understanding outlined in the Introduction. We will also be guided by our previous experience with the dynamics on excited ammonia clusters, which appear indeed to exhibit a number of similarities to the present case as far as internal rearrangement and hydrogen transfer are concerned.[16−18] As a quantitative starting point we will have to rely on the rather scarce spectroscopic data for the indole molecule and the indole−ammonia clusters so far published in the literature,[19,20] which are schematically summarized in Figure 5 . For the energy of the $\pi\sigma^*$ state of indole only the calculated value of 4.88 eV[4] is indicated. The indole−NH_3 binding energy of 0.2 eV is an estimated value with an uncertainty of ±0.1 eV. For indole$(NH_3)_2$ a weak reduction of the vertical ionization potential (IP = 7.20 eV) as well as of its S_1 state energy (4.32 eV) compared to indole(NH_3) has been found.[20] As we shall see in the FEICO electron spectra the energetics of the larger clusters does not change very much.

Our discussion of the dynamics of indole−ammonia clusters after excitation with a pump photon will follow essentially the reaction scheme already proposed in our previous work.[12] As we have seen already in the ion signals emerging from the pump−probe delay scans, warranting a fit with several decay constants, a complex dynamics evolves on the excited-state surface involving internal conversion, hydrogen transfer, rearrangement, and dissociation. Without any more detailed theoretical guidance in exploring the energetics and geometries involved in all these processes, we cannot hope to derive a finally conclusive understanding of the elaborate reaction pathways of the system. We will thus try to discuss our observations and to visualize the energetics and reaction pathways within a plausible kinetic scheme which allows us to describe the experimental results in a consistent manner—being aware that such a model has to remain highly simplified in comparison with the true dynamics on a set of multidimensional potential surfaces with several conical intersections between different electronic states involved. The presently used model is illustrated in Figure 6, indicating very schematically the energetics of the excited- and ionic-state system as well as the energies of the photons and electrons (e) involved on a realistic scale. The numbers in parentheses in the figure refer to the states (or geometries) involved: After the initial excitation by a pump photon $h\nu_{pu}$ from the ground state (1) to the $\pi\pi^*$ state (2), a very fast (time constant τ_2) internal conversion (IC) process occurs—most probably via a conical intersection[9] to the "dark" $\pi\sigma^*$ state (3):

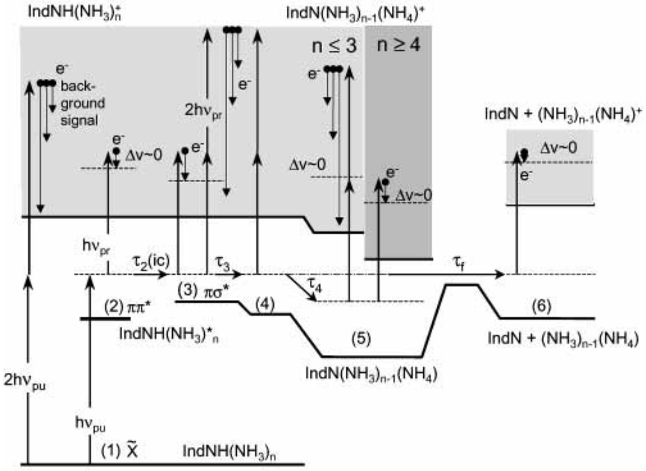

Figure 6. Proposed kinetic model and energetics for the excitation and ionization of small indole ammonia clusters. For details see the text.

$$\xrightarrow{263\text{ nm}} \mathrm{IndNH(NH_3)}_n\,\pi\pi^* \rightarrow \mathrm{IndNH(NH_3)}_n\,\pi\sigma^* \qquad (4)$$

The internal conversion leads to a diffuse distribution of the σ^* electron. The following relocation of the proton and redistribution of the electron density finally leads to an effective H transfer.[9] When state 3 is populated in this manner, it will not be in its equilibrium geometry. The dynamics which follows leads with time constant τ_3 to configuration 4, possibly an initial adjustment of the H atom to a local minimum, followed by an internal rearrangement of the ammonia groups similar to the processes observed in the excited state $(NH_3)_n{}^*(\tilde{A})$.[18] In the present case, these latter processes occur with time constant τ_4 on a picosecond time scale; i.e., geometry 4 is depopulated with τ_4, while on the same time scale geometry $IndN(NH_3)_{n-1}NH_4$ is formed by internal rearrangement of the type

$$\mathrm{IndNH(NH_3)}_n\,\pi\sigma^* \rightarrow \mathrm{IndN\cdots H(NH_3)}_n\,\pi\sigma^* \rightarrow \mathrm{IndN(NH_3)}_{n-1}\mathrm{NH_4} \qquad (5)$$

This latter "state" (5)—a special geometry on the surface with initially $\pi\sigma^*$ character rather than a different electronic state—appears to be stable within our time window of observation as seen in the ion signal delay scans in Figure 2 for $n = 1$ and 2 as well as for the larger clusters in Figure 3.

One might expect a correlation of the temporal behavior of the formation of $IndN(NH_3)_{n-1}NH_4$ (τ_4, state 5) with the formation of the observed $(NH_3)_{n-1}NH_4$ product radicals (τ_f, state 6) according to the reaction scheme (eq 1) discussed in the Introduction. This is obviously not the case as seen by comparing the time constants τ_4 and τ_f given in Table 1 or the respective ion signals in Figures 3g,h and 4a,b.

(i) Clearly, clusters in configuration 5—believed to correspond to the H-transfer state $IndN(NH_3)_{n-1}NH_4$—cannot as a whole be parents of the radicals in the spirit of a kinetic model. The population of state 5 remains constant after its formation (e.g., for $n = 5$ after less than 1 ps), while the formation of $(NH_3)_{n-1}NH_4$ saturates with time constants from 160 to 75 ps. If all $IndN(NH_3)_{n-1}NH_4$ clusters were potential parents, we would expect a constant rise of the $(NH_3)_{n-1}NH_4$ signal from the constant population, even if the fragmentation probability is assumed to be low and the detection probability for the radicals high—the latter due to the large transition dipole moments of the alkali-metal-atom-like electron configuration of NH_4.[21]

(ii) The vastly different time scales observed for the rearrangement processes leading to channel 5—which we attribute to $IndN(NH_3)_{n-1}NH_4$—and for the product formation $(NH_3)_{n-1}NH_4$ also suggest that both species do not have the same direct parent in the sense of a kinetic model (i.e., they cannot originate from the same geometry and rovibrational state population in $\pi\sigma^*$ state 3). Otherwise, the lifetime of the parent would immediately be reflected in the respective formation times.

One possible interpretation of these observations (but by no means the only one) is indicated in Figure 6 by the barrier separating states 5 and 6. The branching occurs already during an early time in the dynamics (in geometry 3 or 4), and only a small fraction of $IndN(NH_3)_{n-1}NH_4$ clusters in the H-transfer state with sufficient energy available in the reaction coordinate may channel from geometry 5 to geometry 6 on the 100 ps time scale.

Note that Figure 6 distinguishes between clusters with $n \leq 3$ and those with $n \geq 4$. This will be discussed in detail in section III.C when we address the pertinent ionization mechanisms for detection of the different states along the reaction path. Here we just mention that the arrows showing the reaction pathways in Figure 6 are allowed to point downward, indicating that energy may be dissipated (i.e., redistributed among the many degrees of freedom of the system) in such a way that it is no longer available for the subsequent ionization mechanism or for dissociation (at least on our time scale of observation).

Finally we point out that, for simplicity and clarity, we have not indicated in Figure 6 any of the various fragmentation processes in the ionic system already mentioned which may occur on a time scale of nanoseconds and can possibly obscure the observed time evolution of ion and electron signals.

C. Analysis of the FEICO Photoelectron Spectra. The FEICO photoelectron spectra discussed below have been measured for the narrow and the broad cluster distributions, in coincidence with the different cluster ions $IndNH(NH_3)_n^+$ (or $IndN(NH_3)_{n-1}NH_4^+$) as well as for one selected radical ion, $(NH_3)_4NH_4^+$. The electron signal as the ordinate of all FEICO spectra represents in random units the number of measured coincident electrons per laser pulse and per energy interval ΔE_{el}. The energy interval usually selected was $\Delta E_{el} = 40$ meV. The number of laser pulses added up at each delay time are not equal; hence, the signal-to-noise ratio of the electron spectra at the various delay times can differ considerably. For different numbers of pump (m) and probe (l) photons absorbed by a cluster we expect different electron kinetic energies up to a maximum corresponding to the excess energy in the ion clusters: $E^{(m,l)}_{exc} = mh\nu_{pu} + lh\nu_{pr} - \mathrm{IP}$. For each case, the maximum electron kinetic energy $E^{(m,l)}_{max}$ observed is $\leq E^{(m,l)}_{exc}$ and only reaches $E^{(m,l)}_{exc}$ if no internal energy remains in the photoion. A first inspection of the photoelectron spectra in Figures 7−15 reveals two distinctive features: a narrow peak at low electron kinetic energies, $0 < E_{el} \leq E^{(1,1)}_{max}$, which we attribute to ionization by one probe photon and a broad, rather structureless distribution with $0 < E_{el} \leq E^{(1,2)}_{max}$ due to ionization with two probe photons. Both contributions appear to have different dynamical behavior and essentially reflect the evolution of Franck−Condon factors as the system evolves after initial excitation to the $S_1(\pi\pi^*)$ state. The data points are connected by full lines; the thin solid lines show a fit by three Gaussian distributions, one for the single-photon ionization while the other two represent the most convenient match to the two-photon ionization contribution. Table 2 summarizes the energetics found from the FEICO spectra discussed in the following sections. Most significant is the jump between $n = 3$ and $n = 4$, indicating a significant change in geometry.

TABLE 2: Summary of the Energetics from the FEICO Photoelectron Spectra for $IndNH(NH_3)_n$[a]

cluster[b]	$E^{(1,1)}_{peak}$/eV	fwhm$^{(1,1)}$/eV	$E^{(1,1)}_{max}$/eV	$E^{(1,2)}_{max}$/eV
IndNH			*c*	3.3[d]
$IndNH(NH_3)$	0.11 ± 0.02	0.18 ± 0.02	0.22[e]	3.4[f]
$IndNH(NH_3)_2$	0.11 ± 0.01	0.18 ± 0.01	0.22	3.0
$IndNH(NH_3)_3$	0.13 ± 0.01	0.22 ± 0.02	0.26	3.0
$IndNH(NH_3)_4$	0.25 ± 0.02	0.29 ± 0.03	0.43	2.3
$IndNH(NH_3)_5$	0.30 ± 0.03	0.33 ± 0.02	0.52	2.4
$(NH_3)_4NH_4$	0.14 ± 0.03	0.17 ± 0.01	0.24	3.0

[a] We report for the one-photon peak seen in the spectra its peak energy, $E^{(1,1)}_{peak}$, and the full width at half-maximum, fwhm$^{(1,1)}$ (both from a Gaussian fit), and the upper energetic limit, $E^{(1,1)}_{max}$, taken somewhat arbitrarily at $1/e^2$ of the maximum peak intensity. Also given is an estimate for the overall maximum energy observed in the spectra, $E^{(1,2)}_{max}$, with an uncertainty of about ±0.2 eV. [b] Spectra taken at delay times $\tau > 2$ ps. [c] Maximum excess energy from the IP (cf. Figure 5): $E^{(1,1)}_{exc} = 0.09$ eV. [d] From the IP: $E^{(1,2)}_{exc} = 3.25$ eV. [e] From the IP: $E^{(1,1)}_{exc} = 0.6$ eV. [f] From the IP: $E^{(1,2)}_{exc} = 3.75$ eV.

For the small clusters $IndNH(NH_3)_n$, $n = 1-3$ (Figures 7−12), a relatively strong background signal is detected at $\tau < 0$ due to absorption of two pump photons alone or three probe photons alone. It was subtracted from the electron spectra at $\tau \geq 0$, causing an increased statistical error. For clusters with $n \geq 4$ the background is significantly smaller.

1. Bare Indole Molecule. We first discuss the FEICO spectra for bare indole (Figure 7). No pronounced electron peak is observed at small electron energies, $E_{el} \leq E^{(1,1)}_{exc} = h\nu_{pu} + h\nu_{pr} - \mathrm{IP} = 0.09$ eV; i.e., photoionization by only one probe photon is significantly less efficient than the corresponding two-probe-photon process, leading to total electron kinetic energies of up to $E^{(1,2)}_{exc} = 3.25$ eV (these maximum excess energies are derived from the IP; cf. Figure 5). This observation is explained by very small Franck−Condon factors for one-photon transitions from the electronically excited state to the ionic ground state (at all delay times probed): with a presumably similar geometry of the S_1 state and the ionic ground state, one expects a "propensity" for the vibrational quantum numbers to remain unchanged ($\Delta v = 0$), i.e., the internal energy to remain constant during the ionization process. Since the excess energy in the excited state is 0.34 eV (see Figure 5) while ionization with one photon would allow for a maximum internal energy of 0.09 eV only, ionization cannot occur. A high Franck−Condon factor could only become possible if the molecular geometry in the excited state would significantly change prior to the ionization process. However, as any dynamics in the excited states leads to a dissipation of energy among different degrees of freedom, the small excess energy available is not sufficient to allow for ionization by a single photon. The indole ion signal thus arises exclusively from ionization by two probe photons as indicated in Figure 7 (after subtraction of the background caused by ionizing the ground state by two pump photons). The energy-integrated electron signal reaches its maximum already at small

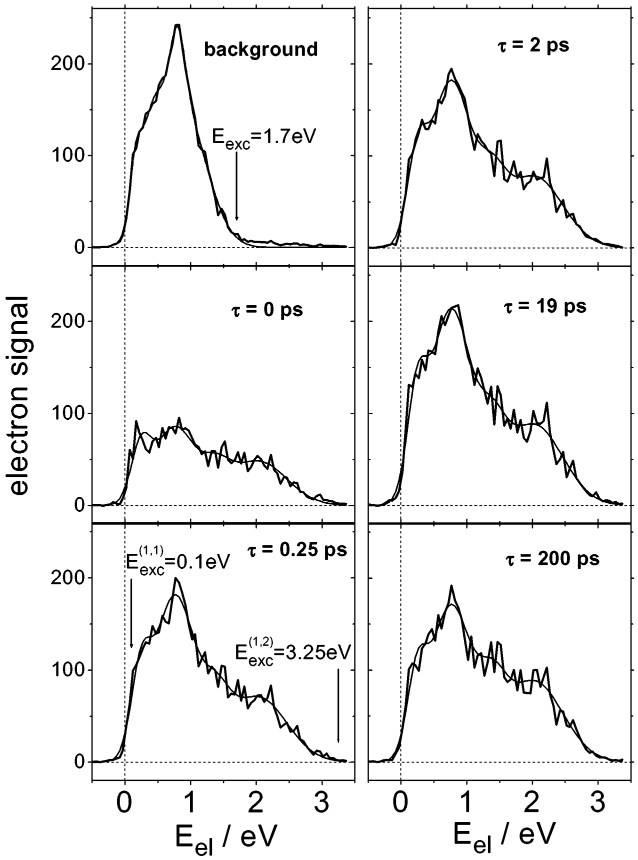

Figure 7. Electron spectra of bare $IndNH^+$ for a narrow cluster distribution ($n \leq 3$) at different delay times τ between pump (263 nm) and probe (395 nm) pulses. The background spectrum at $\tau < 0$ has been subtracted from the spectra at $\tau \geq 0$. The corresponding maximum excess energies estimated from the IP (see Figure 5) are indicated by E_{exc} (for the three-probe-photon background) and $E^{(1,2)}_{exc}$ (for the pump−probe ion signal).

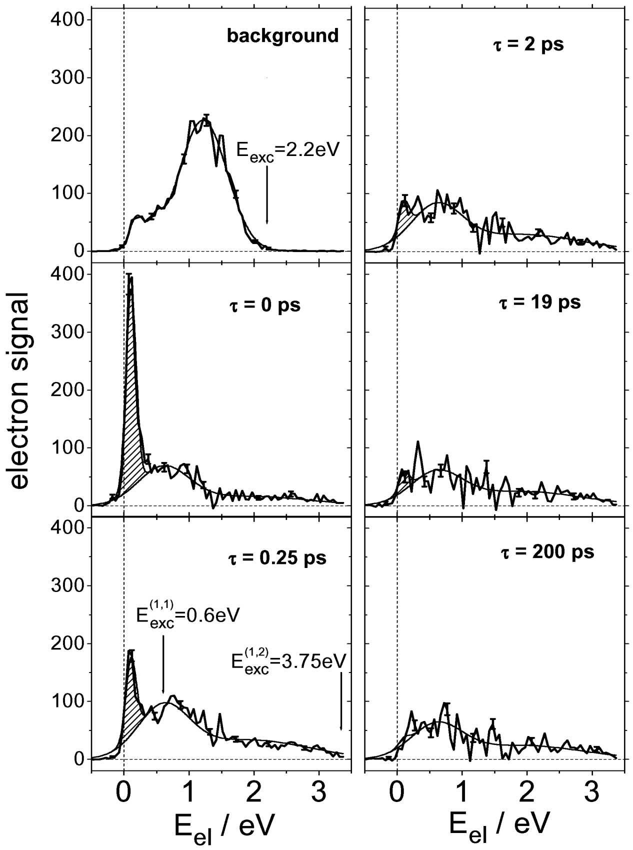

Figure 8. Electron spectra of $IndNH(NH_3)^+$ for a narrow cluster distribution ($n \leq 3$). Otherwise as Figure 7. The corresponding maximum excess energies estimated from the IP (see Figure 5) are indicated by E_{exc} for the three-probe-photon background and $E^{(1,1)}_{exc}$ and $E^{(1,2)}_{exc}$ for the pump−probe ion signal. Error bars indicate typical statistical counting errors.

delay times ($\tau = 0.25$ ps) and stays essentially constant for longer delay times—in agreement with the time-dependent ion signal (cf. parts b and e of Figure 2).

2. Small $IndNH(NH_3)_n$ Clusters, $n = 1-3$. The FEICO spectra of $IndNH(NH_3)_n^+$ for $n = 1-3$ as obtained from a narrow cluster distribution are given in Figures 8−10. In contrast to those of the bare indole molecule they show a strong one-photon peak at low energies peaking at $E_{el} = E^{(1,1)}_{peak} \approx 0.10-0.12$ eV and extending up to 0.35−0.40 eV (see Table 2). For $n = 1$ the total available excess energy amounts to $E^{(1,1)}_{exc} = h\nu_{pu} + h\nu_{pr} - \mathrm{IP} = 0.6$ eV (derived from the IP; cf. Figure 5). The one-photon signal has its maximum at $\tau = 0$, rapidly decreases for $\tau = 0.25$ ps, and vanishes nearly completely for $\tau = 2$ ps. This dynamical behavior is obviously correlated to the ultrafast process observed in the ion signal on the 250 fs time scale (Figure 2c,d). The decay of the one-photon peaks in Figures 8−10 is in agreement with the decay times given in Table 1, although the larger statistical errors do not allow for an independent determination of the lifetimes. The strong signal reflects a good Franck−Condon overlap for one-probe-photon ionization between the initially populated vibrational level of the state and the ionic configuration. This is schematically indicated by the electron arrows in Figure 6. The vibrational energy in the $S_1(\pi\pi^*)$ state (2) is ~0.37 eV (see Figures 5 and 6). If we assume again the excited- and ionic-state geometries to be similar, we expect an ionization process without change of vibrational energy (propensity rule $\Delta v = 0$). In contrast to the bare indole, one probe photon now has sufficient energy to transfer this excitation into the ion and to eject an electron with a kinetic energy of 0.23 eV as illustrated in Figures 5 and 6. Indeed, the experimental photoelectron spectra show a maximum at about 0.1 eV, in good agreement with this consideration and reflecting a rather small change of the internal energy in the ion and hence of the corresponding cluster geometries.

As illustrated by the fit to the ion signal in Figure 2c,d the decay (fit 2) of the $\pi\pi^*$ state (detected via ionization with one probe photon) is accompanied by the growth of a signal (fit 3) presumably originating from an initial configuration in the dark $\pi\sigma^*$ state immediately after internal conversion. As seen in Figure 2, the latter geometry obviously relaxes on a time scale of about 800 fs into configuration 4, which appears to be less efficiently detected (fit 4). The FEICO electron spectra in Figure 8 give us a clear signature on the origin of these latter two signals: ionization by two probe photons gives rise to electron signals also above $E_{el} = 0.6$ eV which extend up to electron energies $E^{(1,2)}_{max} \approx 3.4(2)$ eV for $IndNH(NH_3)^+$. We note, however, that this observed maximum electron kinetic energy is significantly below the excess energy deposited into the molecular ion in the 1 + 2 photon ionization process which we derived from the IP (Figure 5): $E^{(1,2)}_{exc} = h\nu_{pu} + 2h\nu_{pr} - \mathrm{IP} = 3.75$ eV. The observed maximum energies $E^{(1,2)}_{max}$ are even somewhat less for $IndNH(NH_3)_{2,3}{}^+$ as seen in Figures 9 and 10 and summarized in Table 2. Obviously, due to its different electronic structure, the $\pi\sigma^*$ state has no significant Franck−Condon factor for one-photon ionization, and even the two-

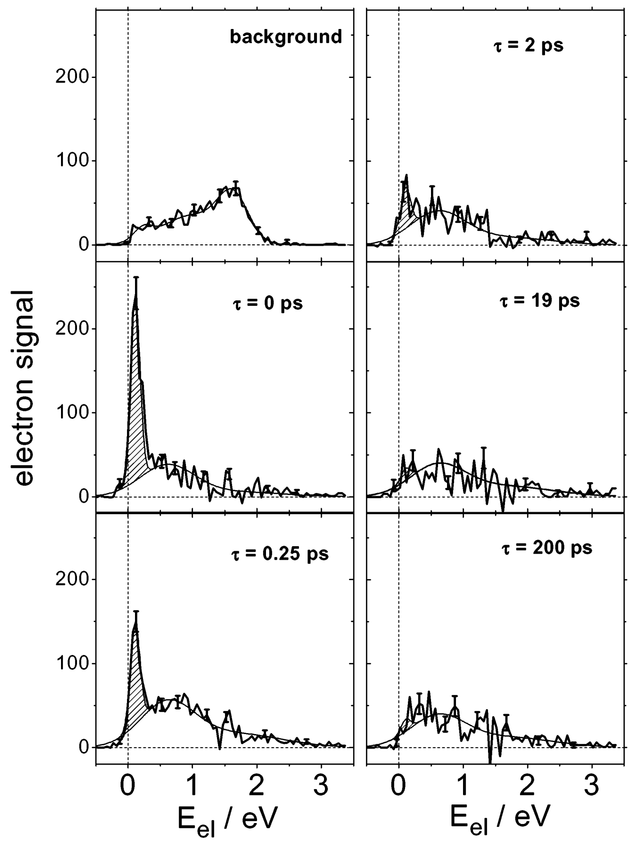

Figure 9. Electron spectra of IndNH$(NH_3)_2^+$ for a narrow cluster distribution ($n \leq 3$). Otherwise as Figure 7.

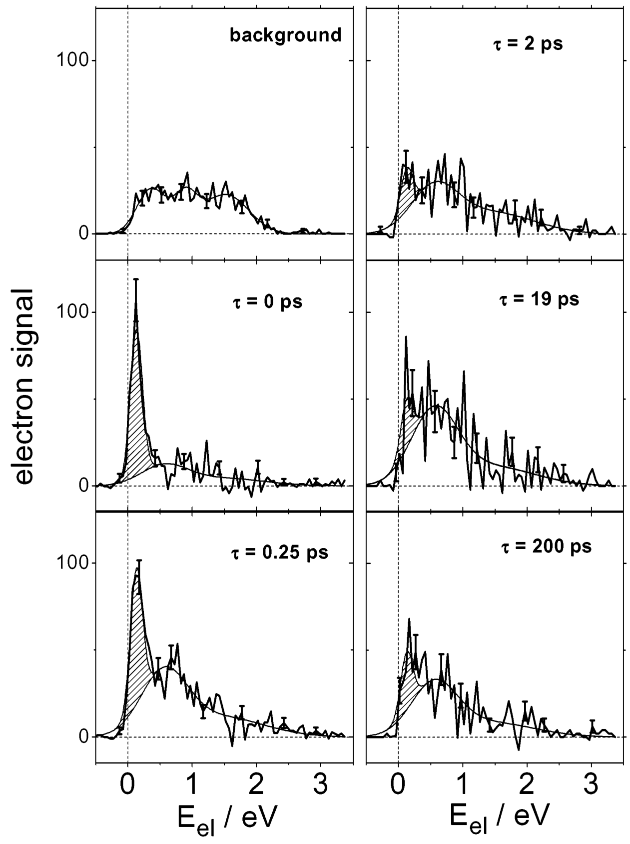

Figure 10. Electron spectra of IndNH$(NH_3)_3^+$ for a narrow cluster distribution ($n \leq 3$). Otherwise as Figure 7.

photon ionization process favors energies significantly above the ionization threshold—especially for cluster sizes $n = 2$ and 3. The FEICO electron spectra do, unfortunately, not allow a distinction between states 3 and 4. Rather, the respective two-photon ionization signal rises from 0 to about 0.25 ps and then very slowly decreases again up to the measurement taken at 200 ps—corresponding to the depopulation of state 4 and the population of state 5 directly reflected by the fit curves in the ion signals (see Figure 2). This decay with time constant τ_4 (picosecond time scale) is attributed in the framework of our kinetic model (Figure 6) to a significant structural rearrangement designated as state 5. The latter geometry (still assumed to belong to the $\pi\sigma^*$ electronic state) may possibly be characterized as IndN$(NH_3)_{n-1}(NH_4)$ and has obviously a nonzero but significantly smaller probability for two-photon ionization than the initial configuration after the $\pi\sigma^*$ state population via the ic process. At present, however, we cannot completely rule out that a crossing of the $\pi\sigma^*$ state potential surface into the ground state may play a role in the decay of the signal. Further elucidation of this process and the role of the H transfer in the heterocluster[9] can be expected from ab initio calculations of the relevant potential energy surfaces and the possible conical intersection between them.[22] In the first results of such calculations for IndNH(NH_3) we have found indeed a high-lying charge-transfer state which might be important, at least for the very small clusters.

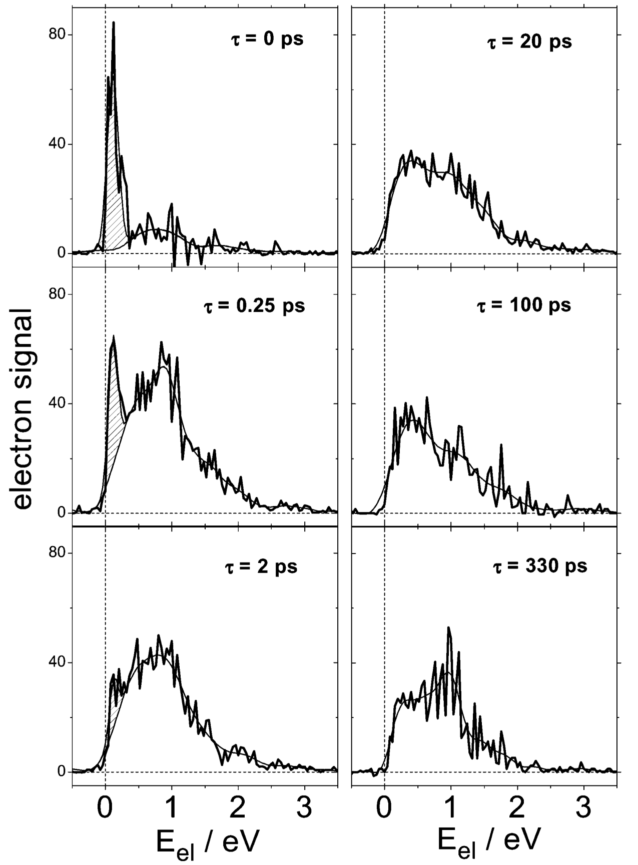

Figure 11. Electron spectra of IndNH$(NH_3)_2^+$ for a broad cluster distribution ($n \leq 6$). Otherwise as Figure 9.

It is interesting to compare the electron spectra for the small clusters IndNH$(NH_3)_{2,3}$ obtained from the narrow cluster distribution (Figures 9 and 10) with those recorded from a broad distribution. The data are shown in Figures 11 and 12. We see a strong increase of the two-probe-photon signal, in particular, at low electron energies, i.e., at high vibrational energies. Thus, these signals can be explained by contributions of larger cluster fragments to the IndNH$(NH_3)_{2,3}^+$ signal: the high excess energy

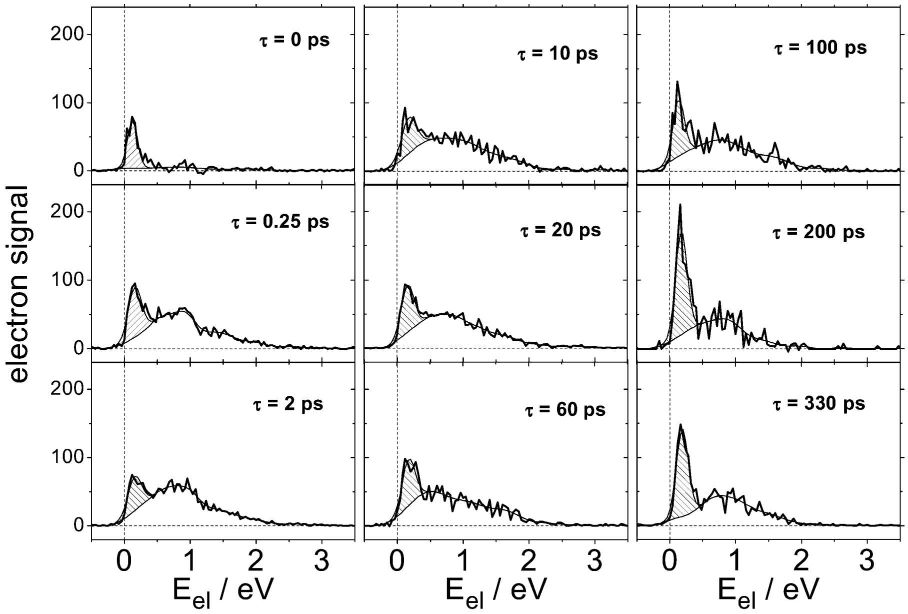

Figure 12. Electron spectra of $IndNH(NH_3)_3^+$ for a broad cluster distribution ($n \leq 6$) at nine different pump−probe delay times. The narrow one-photon ionization peak with its maximum at ca. 0.2 eV now reflects two different processes as indicated by the different shadings (see the text). Otherwise as Figure 10.

in the cluster ions after two-probe-photon absorption leads to the evaporation of NH_3 molecules in the ionic system.

The spectra for $IndNH(NH_3)_3$ (Figure 12) represent a particularly interesting case with the most dramatic differences between broad and narrow (Figure 10) cluster distributions. Apparently, a one-photon ionization signal is detected for short and for longer delay times. This is clearly demonstrated in Figure 12, where the different contributions are again indicated by the respective fits and different shadings. By comparison with Figure 10 it becomes evident that the one-photon peak (low electron kinetic energies) at long delay times arises from fragmentation of larger clusters. This is somewhat surprising as the excess energy in the ion state after one-probe-photon absorption is much less than after two-probe-photon absorption (see above). One possible explanation would be a significantly reduced adiabatic ionization potential for $n \geq 4$ compared to the vertical values. This will be discussed below.

We have integrated the different electron signal contributions of $IndNH(NH_3)_n$ for all cluster sizes from small and large contributions. The decay and rise times τ_i obtained from the ion fits (Table 1) are essentially confirmed by these integrated FEICO spectra, albeit with significantly less accuracy. Nevertheless, for understanding the nature of the different processes observed, the FEICO spectra are instrumental. To illustrate this in a concise manner for one specific example, we display the time dependence of the data derived from the FEICO spectrum for $IndNH(NH_3)_3^+$ in Figure 13. Besides the (i) very fast contribution (peaking within the time steps recorded in the FEICO spectra at about $\tau = 0$), we find (ii) a dominant slowly decaying part caused by two-probe-photon absorption and (iii) a slowly growing part due to one-probe-photon absorption. The superposition of both the slowly varying signals leads to a nearly constant total signal on the picosecond time scale. We attribute the three contributions to (i) one-photon ionization of the $\pi\pi^*$ state, (ii) two-photon ionization of the $\pi\sigma^*$ state, and (iii) one-photon ionization of excited $IndNH(NH_3)_4$ clusters in configuration 5, which is detected on the $IndNH(NH_3)_3^+$ ion channel due to evaporation of NH_3 in the ionic state on the nanosecond time scale. This latter interpretation will become more clear below when the general character of the FEICO spectra for the larger cluster is understood.

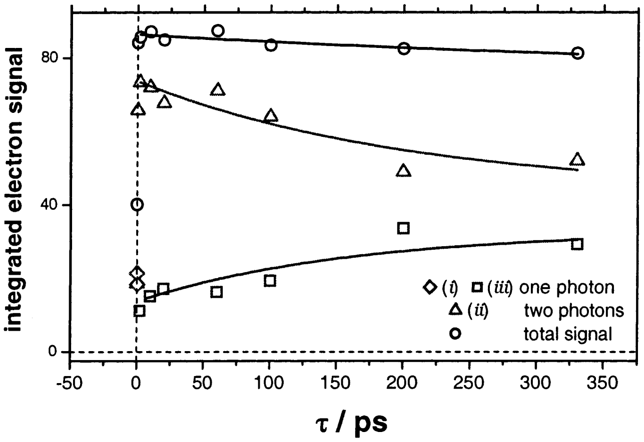

Figure 13. Integrated electron spectra of $IndNH(NH_3)_3^+$ for a broad cluster distribution ($n \leq 6$) versus delay time τ according to Figure 12. The total signal (○) is the sum of the electron signals obtained from ionization by one probe photon [(i) (◇) very fast and (iii) (□) slowly rising processes] and two probe photons [(ii) (△) slow decay]. The very fast signal contribution (i) near $\tau = 0$ is not resolved on the long time scale displayed here.

We have also studied the role of two-photon ionization processes in some detail by repeating the measurement of the FEICO spectra with slightly increased pump pulse intensity but with a probe pulse intensity which was reduced by nearly a factor of 3. This results in a dramatic decrease of the two-photon signal relative to the one-photon signal and hence gives clear evidence of the two-photon character of these processes. However, no quantitative conclusions can be drawn from these observations, and hence, we refrain here from showing the results.

3. $IndNH(NH_3)_n$ Clusters with $n \geq 4$. In comparison to the small clusters, $n \leq 3$, an apparently rather different behavior is observed for the electron spectra of $IndNH(NH_3)_n^+$, $n \geq 4$ (see Figures 14 and 15 for $n = 4$ and 5). In particular, for $IndNH(NH_3)_4$ the background signal is extremely weak compared to

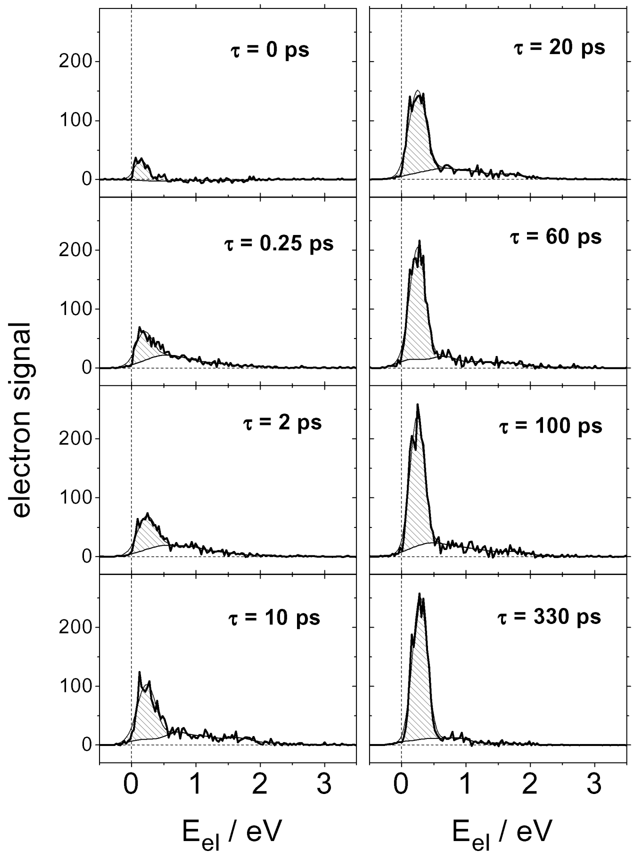

Figure 14. Electron spectra of IndNH$(NH_3)_4^+$ for a broad cluster distribution ($n \leq 6$). Otherwise as Figure 7.

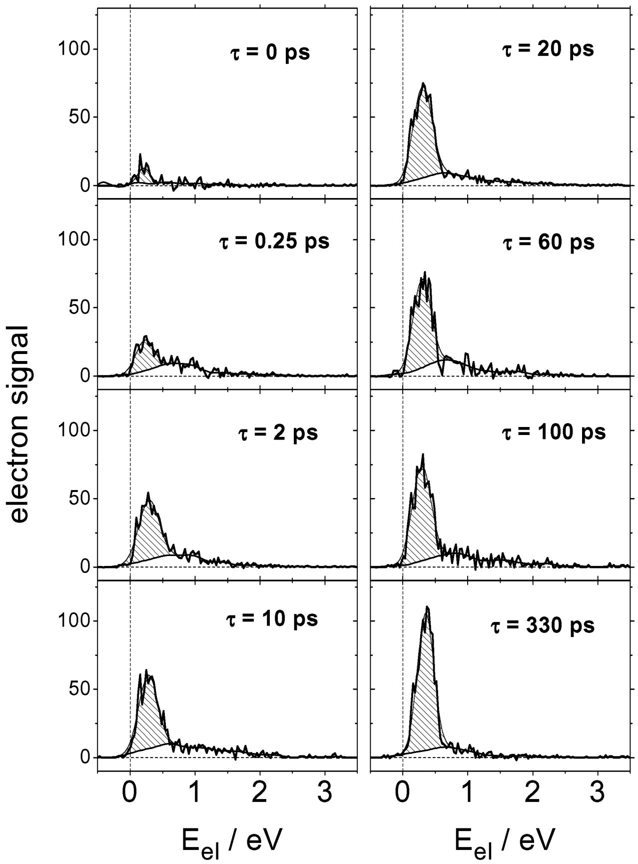

Figure 15. Electron spectra of IndNH$(NH_3)_5^+$ for a broad cluster distribution ($n \leq 6$). Otherwise as Figure 7.

the large signals for $n \leq 3$. As the background signals represent vertical transitions from the ground to the ion states the corresponding Franck–Condon factors for these transitions decrease strongly from $n = 4$ to $n = 3$, reflecting large geometrical changes of the corresponding states for these cluster sizes. The electron spectrum at $\tau = 0$ shows only a very small signal (the residual contribution of false coincidences has again been subtracted), and also for $\tau = 0.25$ ps only a relatively small one-probe-photon signal is observed. Thus, for short delay times the transition probability to the ionic state is rather inefficient. Probably, the cluster geometry in the initially excited $\pi\pi^*$ electronic state differs strongly from that of the lowest ionic state, causing a low Franck–Condon factor for ionization. Also the two-photon ionization process is less efficient in ionizing the $\pi\sigma^*$ state in its initial geometry. Nevertheless, we may safely assume that the excited electronic states of these clusters are populated as efficiently as in the case of the smaller clusters. This is documented by the signal at longer delay times above 2 ps, where a strong one-photon ionization electron signal rises in the energy range $0 \leq E_{el} \leq 0.65$ eV. At $\tau = 60$ ps this is the dominant part of the electron spectra, it has essentially reached its maximum value, and it stays approximately constant over the whole observation region, in agreement with the time-dependent ion signal (cf. Figure 3g). Apparently, one-photon ionization becomes again accessible as the dynamics on the excited-state surfaces proceeds: here too, this rise of the FEICO spectra reflects a very efficient Franck–Condon overlap for the one-probe-photon ionization process. We interpret this speciality of the larger clusters as a fingerprint of a significant structural rearrangement of the clusters on the picosecond time scale which forms a particular stable final geometry (stable on a time scale of several hundred picoseconds). This is illustrated in Figure 6 by the energetics shown in the light gray inset labeled $n \geq 4$. Assuming for these clusters a significant drop of the adiabatic ionization potential and nearly equal geometry in the stabilized excited neutral IndN$(NH_3)_{n-1}(NH_4)$ configuration (state 5) and in the corresponding ion, we can again expect a propensity for the vibrational quantum numbers to remain unchanged in the ionization process ($\Delta\upsilon = 0$). As seen from the energetics schematically indicated in Figure 6 we expect thus one-photon ionization to be possible for $n \geq 4$ in contrast to the situation assumed for $n \leq 3$, where obviously $\Delta\upsilon = 0$ cannot be reached with one probe photon. From a theoretical point of view it is plausible that for the ion state of the larger clusters ($n \geq 4$) the charge-transfer geometry IndN$(NH_3)_{n-1}NH_4^+$ corresponding to the H-transfer geometry IndN$(NH_3)_{n-1}NH_4$ is the most stable one, which explains the good Franck–Condon factor in this case. For the ground state the charge-transfer geometry is evidenced only for larger clusters ($n \geq 7$).[13]

4. Formation of $(NH_3)_{n-1}NH_4$ Radicals. As discussed above, the picosecond dynamics of the parent clusters reflects their structural rearrangement on the $\pi\sigma^*$ potential surface after the initial H transfer to the IndN$(NH_3)_{n-1}(NH_4)$ geometry (state 5). One might thus expect the radical products to be formed from this geometry whenever sufficient available excess energy is collected (statistically) in the reaction coordinate for the dissociation process according to eq 1. However, as state 5 remains stable on the time scale presently under observation, e.g., for $n = 5$ at times from about 1 ps up to a few 100 ps, the radicals formed within about 100 ps cannot be a product of state 5. This argument holds even if we assume that only a small fraction of the excited neutral clusters form radicals on the time scale presently discussed (the radicals are very efficiently detected due to the large transition dipole moment for ionization). A closer inspection of the radical formation times τ_f shows,

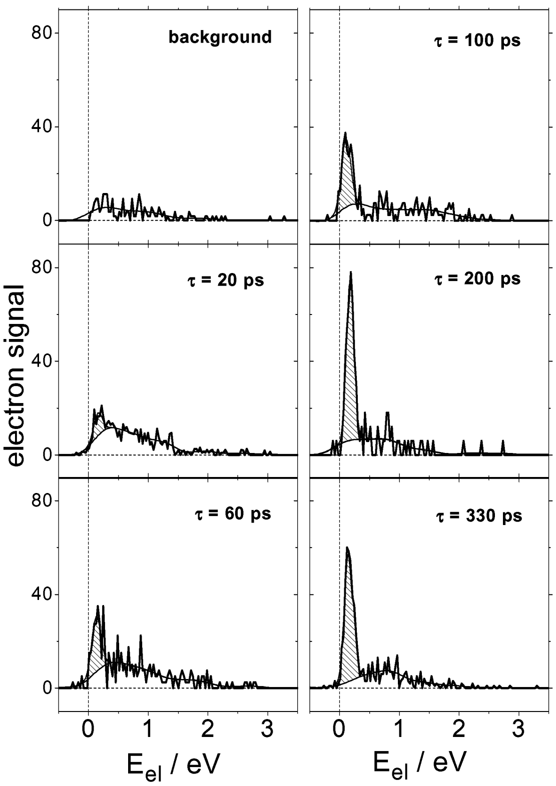

Figure 16. Electron spectra of $(NH_3)_4NH_4^+$ from a broad cluster distribution ($n \leq 6$). Otherwise as Figure 7.

as already reported in refs 12 and 13 and summarized presently in Table 1, for the products of $n = 2-6$ values from $\tau_f = 160$ ps to $\tau_f = 75$ ps. In any case τ_f is substantially larger than the respective τ_4, the decay time of state 4 and formation time of state 5. Hence, the two channels also cannot have the same direct parent in a kinetic model. In other words, the radicals are formed via a pathway different from that leading to the stable internal rearrangement. A further intermediate geometry and a barrier may be involved as indicated on the right side of Figure 6. The corresponding FEICO photoelectron spectra for the example of $(NH_3)_4NH_4^+$ are displayed in Figure 16 (similar data are obtained for other fragments). The rise time of the photoelectron signal is ~80 ps, which is consistent with the value derived from the ion traces (Table 1). The photoelectron peak shows very low electron kinetic energies, which can be rationalized by arguments similar to those used for the one-photon signal at long delay times observed for parent clusters with $n \geq 4$, i.e., as due to a propensity for $\Delta v = 0$. Since Figure 6 is drawn to scale wherever the energetics is known, we can directly derive the observed electron energy from that schematic. The difference between the probe photon energy of 3.14 eV and the ionization potential of $(NH_3)_4NH_4$ of 2.73 eV[21] is 0.41 eV, which would be the electron energy if the relation $\Delta v = 0$ holds. In fair agreement the experiment shows a peak maximum at 0.2 eV, and electron energies reach up to 0.40 eV.

IV. Conclusions

Time-resolved photoelectron spectroscopy of excited indole–ammonia clusters with the FEICO method gives deep insight into the processes evolving after exciting the $\pi\pi^*$ state of the indole chromophore. Whereas the time constants of the dynamical processes in the excited indole$(NH_3)_n$ clusters can be derived more accurately from time-dependent ion signals, the electron spectra allow us in principle to follow the evolution of the excited systems on the potential energy surfaces and to analyze the essential steps of the reaction such as internal conversion, H transfer, structural changes, vibrational relaxation, and dissociation. In particular, the primary ultrafast internal conversion—directly visible for the small clusters ($n \leq 3$)—has also been deduced for the larger clusters ($n \geq 4$) for which this process is not detectable in the ion signals. By assignment of the subsequent processes of the H transfer and structural rearrangement, the existence of the primary step has been unambiguously confirmed. The different contributions to the parent ion signals resulting from ionization by one- and two-probe-photon absorption can be clearly separated.

The interpretation of the photoelectron spectra essentially confirms the previously suggested dynamical model[3,9,12] of the H-transfer reaction in indole–ammonia clusters and allows us a more detailed, albeit schematic, kinetic modeling of the relevant processes outlined in the paper and summarized in Figure 6. We believe that these findings may be of general relevance for photoinduced reactions in such biologically relevant molecular systems. Some uncertainties remain with respect to an unambiguous assignment of certain process steps along the reaction path. With respect to the internal conversion from the initial excited state to the subsequently populated electronic state within a few hundred femtoseconds, we now strongly favor the assumption of a $\pi\pi^* \rightarrow \pi\sigma^*$ transition to be effective in accordance with the theoretical predictions. The subsequent H atom transfer causes a structural rearrangement of the excited clusters on the time scale of several tens of picoseconds to several hundred picoseconds. During this rearrangement an alternative, weak channel leads to dissociation on a time scale of 80–140 ps. Comparing the electron spectra of small indole$(NH_3)_n$ clusters ($n \leq 3$) with those for larger clusters ($n \geq 4$), a relatively strong change of their qualitative behavior is observed which can be explained by a significantly reduced adiabatic ionization potential and a rearranged IndN-$(NH_3)_{n-1}(NH_4)$ geometry for $n \geq 4$, which is favorable for one-photon ionization. Comparison of the results for broad and narrow cluster distributions demonstrates the influence of ionic fragmentation (NH_3 evaporation) at the nanosecond time scale on the observed (femtosecond and picosecond) time-dependent ion and electron signals of smaller clusters. It has, however, been shown that the main findings are not significantly modified. Reduction of the cluster size distribution can almost eliminate these effects. We finally mention that the first preliminary results from experiments with deuterated indole–ammonia clusters are under way in our laboratory. They reveal for the parent clusters a negligible isotope effect on the short time scale (τ_2 and τ_3) but a significant effect at longer delay times (τ_4). This still relatively small effect on the product formation times (below a factor of 2) can be explained by the modified IVR processes which accompany the rearrangement of the cluster geometry. The first experiments with a variation of the pump wavelength in the interval from 258 to 274 nm have led to only small changes of the cluster dynamics. Future experiments in an extended tuning range of the excitation energy promise further essential information about the energetics and dynamics of the H-transfer reaction in indole–ammonia clusters. To find an unambiguous confirmation of the presently detailed kinetic model, we will need ab initio calculations of the relevant potential energy surfaces.

Acknowledgment. We thank Dr. F. Noack for his support by providing the laser system in the Femtosecond Application Laboratory of the Max Born Institute. Financial support by the

Deutsche Forschungsgemeinschaft through Sonderforschungsbereich 450 is gratefully acknowledged.

References and Notes

(1) Grossweiner, L. I.; Swenson, G. W.; Zwicker, E. F. *Science* **1963**, *141*, 805.

(2) Peon, J.; Hess, G. C.; Pecourt, J.-M. L.; Yuzawa, I.; Kohler, B. *J. Phys. Chem. A* **1999**, *103*, 2460.

(3) Sobolewski, A. L.; Domcke, W. *Chem. Phys. Lett.* **1999**, *315*, 293.

(4) Sobolewski, A. L.; Domcke, W. *Chem. Phys. Lett.* **2000**, *329*, 130.

(5) Dian, B. C.; Longarte, A.; Zwier, T. *J. Chem. Phys.* **2003**, *118*, 2696.

(6) Sobolewski, A. L.; Domcke, W. *J. Phys. Chem. A* **2001**, *105*, 9275.

(7) Pino, G. A.; Dedonder-Lardeux, C.; Grégoire, G.; Jouvet, C.; Martrenchard, S.; Solgadi, D. *J. Chem. Phys.* **1999**, *111*, 10747. Pino, G.; Grégoire, G.; Dedonder-Lardeux, C.; Jouvet, C.; Martrenchard, S.; Solgadi, D. *Phys. Chem. Chem. Phys.* **2000**, *2*, 893. Grégoire, G.; Dedonder-Lardeux, C.; Jouvet, C.; Martrenchard, S.; Peremans, A.; Solgadi, D. *J. Phys. Chem. A* **2000**, *104*, 9087.

(8) Ishiuchi, S.; Sakai, M.; Daigoku, K.; Ueda, T.; Yamanaka, T.; Hashimoto, K.; Fujii, M. *Chem. Phys. Lett.* **2001**, *347*, 87. Ishiuchi, S.; Daigoku, K.; Saeki, M.; Sakai, M.; Hashimoto, K.; Fujii, M. *J. Chem. Phys.* **2002**, *117*, 7077. Ishiuchi, S.; Daigoku, K.; Saeki, M.; Sakai, M.; Hashimoto, K.; Fujii, M. *J. Chem. Phys.* **2002**, *117*, 7083.

(9) Sobolewski, A. L.; Domcke, W.; Dedonder-Lardeux, C.; Jouvet, C. *Phys. Chem. Chem. Phys.* **2002**, *4*, 1093.

(10) Dedonder-Lardeux, C.; Grosswasser, D.; Jouvet, C.; Martrenchard, S.; Teahu, A. *Phys. Chem. Chem. Phys.* **2001**, *3*, 4316.

(11) Zwier, T. S. *J. Phys. Chem. A* **2001**, *105*, 8827.

(12) Stert, V.; Hesse, L.; Lippert, H.; Schulz, C. P.; Radloff, W. *J. Phys. Chem. A* **2002**, *106*, 5051.

(13) Lippert, H.; Stert, V.; Hesse, L.; Schulz, C. P.; Radloff, W.; Hertel, I. V. *Eur. Phys. J. D* **2002**, *20*, 445.

(14) Stert, V.; Radloff, W.; Schulz, C.-P.; Hertel, I. V. *Eur. Phys. J. D* **1999**, *5*, 97.

(15) Freudenberg, Th.; Radloff, W.; Ritze, H.-H.; Stert, V.; Weyers, K.; Noack, F.; Hertel, I. V. *Z. Phys. D* **1996**, *36*, 349.

(16) Farmanara, P.; Stert, V.; Ritze, H.-H.; Radloff, W.; Hertel, I. V. *J. Chem. Phys.* **2001**, *115*, 277.

(17) Farmanara, P.; Ritze, H.-H.; Stert, V.; Radloff, W.; Hertel, I. V. *Eur. Phys. J. D* **2002**, *19*, 193.

(18) Farmanara, P.; Ritze, H.-H.; Stert, V.; Radloff, W.; Hertel, I. V. *J. Chem. Phys.* **2002**, *116*, 1443.

(19) Carney, J. R.; Zwier, T. S. *J. Phys. Chem. A* **1999**, *103*, 9943.

(20) Hager, J.; Ivanco, M.; Smith, M. A.; Wallace, S. C. *Chem. Phys.* **1986**, *105*, 397.

(21) Fuke, K.; Takasu, R.; Misaizu, F. *Chem. Phys. Lett.* **1994**, *229*, 597.

(22) Ritze, H.-H.; et al. To be published.